Canards, Clusters, and Synchronization in a Weakly Coupled Interneuron Model

2 authors:

Bard Ermentrout
University of Pittsburgh
439 PUBLICATIONS   **30,141** CITATIONS

Martin Wechselberger
The University of Sydney
81 PUBLICATIONS   **3,195** CITATIONS

Some of the authors of this publication are also working on these related projects:

Applied Mathematics View project

Mathematics View project

CANARDS, CLUSTERS AND SYNCHRONIZATION
IN A WEAKLY COUPLED INTERNEURON MODEL

BARD ERMENTROUT[*] AND MARTIN WECHSELBERGER[†]

Abstract. Applying a low current to a recent biophysical model for inhibitory neurons in the cortex leads to mixed mode oscillations (MMOs), a mixture of spikes and subthreshold oscillations. At higher currents, the neurons fire regularly. We show that a specific slow potassium current underlies this behavior. Next we reduce this five-dimensional biophysical model for an inhibitory neuron to three dimensions with a slow/fast time-scale structure. We then show that there is a range of parameters under which the reduced model shows MMOs which can be explained by the canard phenomenon. Many inhibitory interneurons are coupled with electrical tight junctions (gap junctions). We show that such coupling combined with the underlying MMOs produces clustered solutions in large networks. We explain this using the thoery of weakly coupled oscillators and show that the complex dynamics arises from sensitivity near the canard.

1. Introduction. Electrical coupling via gap junctions is widespread in networks of cortical inhibitory neurons [18, 38]. The effects of such electrical coupling has been the focus of much experimental and theoretical work [18, 38], [9, 41, 37, 15, 33]. Most experimental and theoretical findings show that electrical coupling can help to coordinate synchronous oscillatory behaviour in inhibitory networks. Many of the studies of gap junction coupling and oscillations concern pairs of cells (e.g. [38, 37, 17, 41]) rather than larger networks. Synchrony is not the only possibility when coupling via gap junctions and both the shape of spikes [9] and the intrinsic dynamics [41] can destabilize synchronization. Combinations of gap junctions with inhibitory coupling can lead to more complex behavior such as waves [26] and clusters [40, 26] or can enhance the ability to synchronize [37, 33]. Clustered behavior in networks of oscillators often arises when there is multistability in pairwise interactions (although this is not a requirement) and there have been numerous studies of such behavior in oscillator networks [26, 28, 19, 1, 8, 3].

In this paper, we explore the relationship between intrinsic dynamics, coupling and patterns of synchrony for a recently proposed interneuron model [13] endowed with a slow potassium channel. We will focus on the formation of clusters and synchronization in a network of electrically coupled interneurons. We first show, via numerical simulations that at low currents and with weak coupling, these networks organize themselves into clustered states that persist even in the presence of a small amount of noise. At higher currents, the networks become synchronous. In order to understand the mechanism by which there is a transition from clustering to synchrony, we first examine the single cell model. We find that at low currents, there are so-called mixed-mode oscillations (MMOs) [6], an alternation of subthreshold oscillations with spiking activity. Thus, we first turn our attention to the analysis of this behavior. By reducing the system of five differential equations to one that has three with a slow/fast time-scale structure, we are able to show that the underlying dynamics is due to the presence of a canard structure [4, 46, 49, 7, 50, 10, 24, 22, 5, 39].

---
[*]Department of Mathematics, University of Pittsburgh, PA
[†]School of Mathematics & Statistics, Centre of Mathematical Biology, University of Sydney, NSW, Australia

Such canard induced MMOs have been identified in other neuronal models as well [12, 43, 44, 11, 23, 45, 34, 42]. Next, we use weak coupling theory to analyze the weakly coupled network. The connection between the canards and the clustering is through the complex response of individual neural oscillators to perturbations (the adjoint of the linearized dynamics) which makes the weak interaction between oscillators very complicated. As we discuss later in the paper, the key requirement for the formation of two or more clusters is that the phase-interaction function be dominated by higher order odd Fourier modes [36]. The underlying MMOs cause the emergence of such modes and thus the appearance of robust clusters.

The paper is organized as follows: In Section 2 we present the Erisir model and show numerical observations of MMOs, clustering and synchronization. In Section 3 we perform a single cell analysis to explain MMOs via the canard phenomenon. In Section 4 we use weak coupling theory to show that the canard structure is responsible for clustering in an inhibitory network. Finally, we conclude in Section 5.

2. The Erisir model.

2.1. Single cell. The single cell Erisir model [13] is a conductance-based model of a fast-spiking (FS) cortical interneuron. (We remark that in the original Erisir reference, there are typographical errors in the description of the equations. We are using the version of the model in [38].) The ionic currents of the Erisir model consist of a fast sodium current I_{Na}, two potassium currents, a 'moderate' delayed rectifier I_K associated with a $K_v3.1$ ion channel and a 'slow' delayed rectifier I_{Ks} associated with a $K_v1.3$ ion channel, and a passive leak current I_L. The model equations are:

$$\begin{array}{rcl}
C\,V' & = & I_{app} - (I_{Na} + I_K + I_{Ks} + I_L)\,, \\
x' & = & (x_\infty(V) - x)/\tau_x(V)\,, \qquad x = m, h, n, s\,,
\end{array} \tag{2.1}$$

where C is the capacitance of the FS interneuron, I_{app} is an applied (external) current,

$$\begin{array}{rcl}
I_{Na} & = & g_{Na}\,m^3 h(V - E_{Na})\,, \\
I_K & = & g_K\,n^2(V - E_K)\,, \\
I_{Ks} & = & g_{Ks}\,s^4(V - E_K)\,, \\
I_L & = & g_L\,(V - E_L)
\end{array} \tag{2.2}$$

are the ionic currents, where m is the activation gate and h is the inactivation gate of the sodium current, n is the activation gate of the I_K potassium current and s is the activation gate of the I_{Ks} potassium current. The dynamics of each gate $x = m, h, n, s$ is towards the steady state voltage dependent sigmodial function $x_\infty(V)$ with the characteristic voltage dependent bell-shaped time constant $\tau_x(V)$. The parameters g_y ($y = Na, K, Ks, L$) and E_z ($z = Na, K, L$) are conductances and Nernst potentials of the various ionic currents. All parameters and functions are defined in the Appendix A.

Figure 2.1 shows the bifurcation diagram of the single cell Erisir model (2.1) where the bifurcation parameter is the applied current I_{app} (in pA/cm^2). The cell is excitable for $I_{app} < I_{Hopf}$ where $I_{Hopf} \approx 0.64$ denotes a supercritical Hopf bifurcation. The corresponding limit cycle loses stability at $I_{app} \approx 0.65$ due to a subcritical period-doubling bifurcation which opens a parameter window up to $I_{app} = I_{snlc} \approx 0.73$ with apparently no stable simple attractors. I_{snlc} denotes a saddle-node bifurcation of limit cycles. For $I_{app} > I_{snlc}$ there exist large relaxation type oscillations.
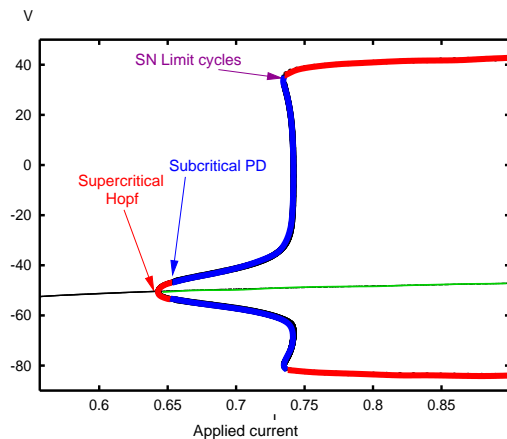
FIG. 2.1. *Bifurcation diagram of Erisir model (2.1): Bifurcation parameter is the applied current I_{app}; supercritical Hopf bifurcation for $I_{app} \approx 0.64$; for $I_{app} \approx 0.65$ limit cycle loses stability at a sub-critical period-doubling bifurcation; $I_{app} \approx 0.73$ saddle-node of limit cycles occurs. Stable periodic orbits are red, unstable blue; stable fixed points are black, unstable are green.*
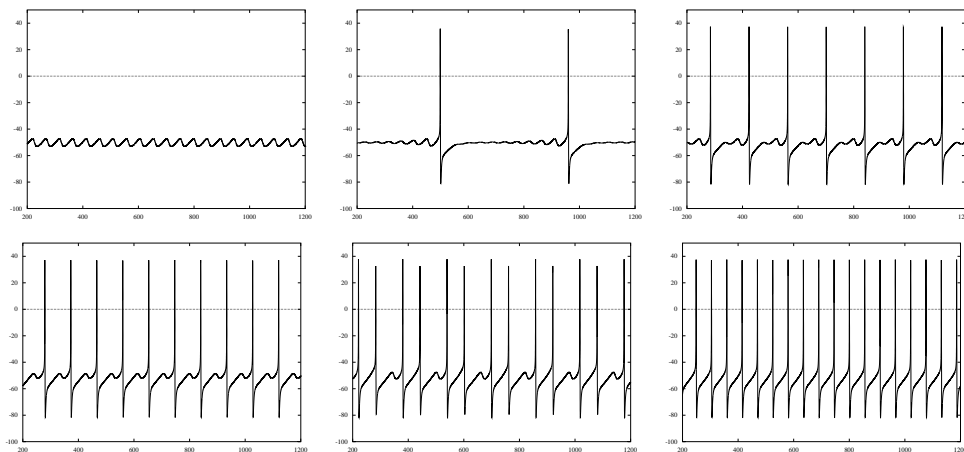

FIG. 2.2. *Voltage time traces of Erisir model (2.1): Upper/Left: small oscillatory pattern 0^1 for $I_{app} = 0.65$; Upper/Middle: MMO pattern 1^9 for $I_{app} = 0.66$, Upper/Right: MMO pattern 1^2 for $I_{app} = 0.70$; Bottom/Left: MMO pattern 1^1 for $I_{app} = 0.72$; Bottom/Middle: MMO pattern 2^1 for $I_{app} = 0.73$, Bottom/Right: relaxation oscillation pattern 1^0 for $I_{app} = 0.74$;*

What are the attractors, if any exist, in this parameter window between small amplitude subthreshold oscillations (STOs) and large amplitude relaxation type oscillations (ROs)? Figure 2.2 shows time traces for several values of applied current I_{app}. STO patterns lose stability for $I_{app} \approx 0.654$ and MMO patterns show up as stable solutions for the Erisir model filling the gap of stable solutions in Figure 2.1. The simplest periodic MMO patterns are of the form L^s, where L denotes the number of ROs and s denotes the number of STOs. For example, Figure 2.2 shows MMO patterns of the form 1^9, 1^2, 1^1 and 2^1. STOs only can be viewed as a 0^1 MMO pattern while ROs only can be viewed as 1^0 MMO patterns. Under the variation of the bifurcation
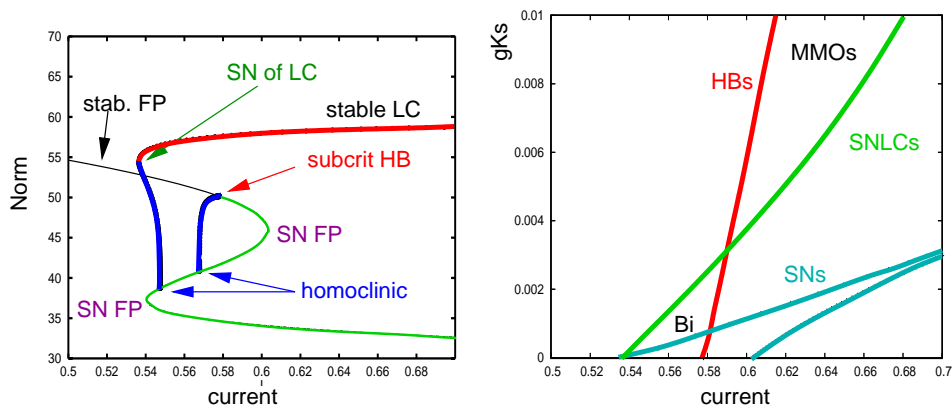
FIG. 2.3. *(A) Bifurcation diagram of Erisir model (2.1) when $g_{Ks} = 0$ as current varies. Instead of membrane potential, the L_2 norm of the solution is plotted as it produces a clearer picture. Colored curves as in figure 2.1. (B) Two parameter diagram showing the branch of Hopf bifurcations (HBs, red), saddle-nodes of fixed points (cyan) and saddle-nodes of limit cycles (SNLCs,green). g_{Ks} for figure 2.1 is 0.018 which is out of the picture. In the region labeled "Bi" between the HBs and the SNLCs, there is bistability between fixed points and large amplitude limit cycles. Mixed mode oscillations are found in the region labeled "MMOs".*

parameter I_{app} one observes the following sequence of simple MMO patterns:

$$0^1 \rightarrow 1^{s_*} \rightarrow \cdots \rightarrow 1^1 \rightarrow 2^1 \rightarrow \cdots \rightarrow L_*^1 \rightarrow 1^0$$

where s_* can be an arbitrary large integer and L_* is a finite upper bound. More complicated MMO patterns are also possible and can be usually found in the transition from one to another simple MMO pattern. In Section 3 we will show that these MMO patterns can be explained by the canard phenomenon [7, 49].

Before turning to the coupling between such cells and our analysis of the canard phenomenon, we remark that there are several other models for inhibitory interneurons, e.g., the Wang-Buzsaki (WB) model [48] which do not seem to have any MMOs. Notably absent in the WB model is the g_{Ks} channel. If we set this current to zero in the Erisir model, the bifurcation from rest to repetitive oscillations is considerably simpler and resembles the sequence in Izhikevich (2006) [31] (figure 6.40, page 197). The recent model in [20] is like the Erisir model but without the slow potassium current and instead an A-type potassium current. This model, too, has no MMOs, at least in the parameters used by the authors. Figure 2.3A shows the corresponding diagram to Figure 2.1 with the norm of the solution plotted for clarity. The Hopf bifurcation (HB) is subcritical and terminates on a homoclinic. The large amplitude limit cycle (red) is lost via a collision with an unstable limit cycle (blue) (saddle-node of limit-cycles; SNLC). The unstable limit cycle is lost at a homoclinic. Between the SNLC and HB, the system is bistable.

Figure 2.3B shows the two-parameter bifurcation diagram. Note that there is only one fixed point for g_{Ks} larger than about 0.004. At $g_{Ks} \approx 0.0035$, the curve of SNLCs (shown in green) crosses to the right of the curve of HBs. In this region there are neither stable fixed points nor large amplitude limit cycles. For small ranges of the applied current and for g_{Ks} larger than about 0.0045, there are stable small amplitude limit cycles, but, the region is primarily dominated by mixed mode oscillations. Indeed, the absence of a large amplitude limit cycle and a stable fixed point is
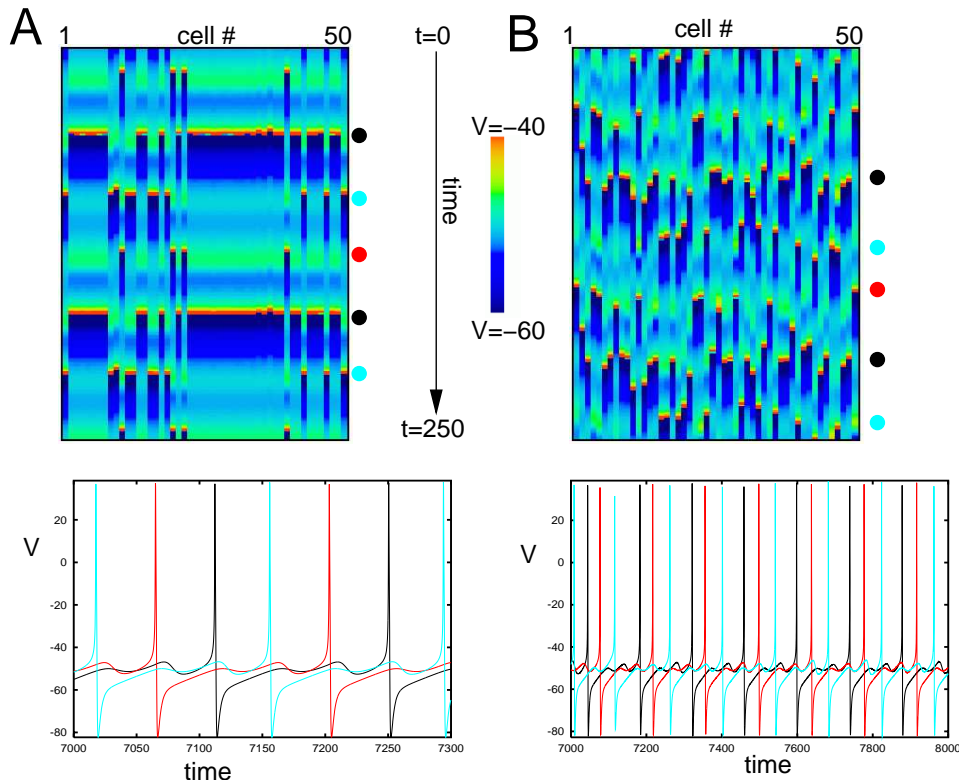
FIG. 2.4. *Simulation of 50 globally gap-junctionally coupled cells with $I_{app} = 0.7$, $g_{Ks} = 0.018$, $g_{gap} = 0.0002$ with no noise, (A) and with $\sigma = 0.002$ amount of Gaussian noise, (B). Top figures show the membrane potential of all 50 cells over a short time span (time goes down). Filled circles show different groups of cells forming clusters that are nearly synchronized. Lower figures show the voltage traces for representative cells in each cluster. This structure is robust to noise.*

a necessary condition for MMOs. The Hopf bifurcation occurring on the lower branch has a somewhat complex structure. For g_{Ks} larger than about 0.0095, the bifurcation is supercritical and thus small amplitude oscillations stably bifurcate from rest. However, in the interval $0.0045 < g_{Ks} < 0.0095$, while the bifurcation is subcritical, the small amplitude unstable branch turns around and gives birth to an interval of stable small amplitude oscillations.

Thus, in this section, we have shown that the slow potassium current appears to be crucial to get mixed mode oscillations. In the next sections we see what are the consequences of this for weakly gap-junctionally coupled cells and then, we show that the mechanism for MMOs is a generalized canard phenomenon.

2.2. Clustering and coupling. Cortical interneurons are usually coupled via gap junctions and GABAergic (inhibitory) synapses. To get a better understanding of clustering and synchrony properties of networks of interneurons we focus in this work on networks with gap junctions only as the issues of time scales and reversal potential no longer play a role [32, 47, 51].

We study a network of cortical interneurons by using the Erisir model (2.1) with
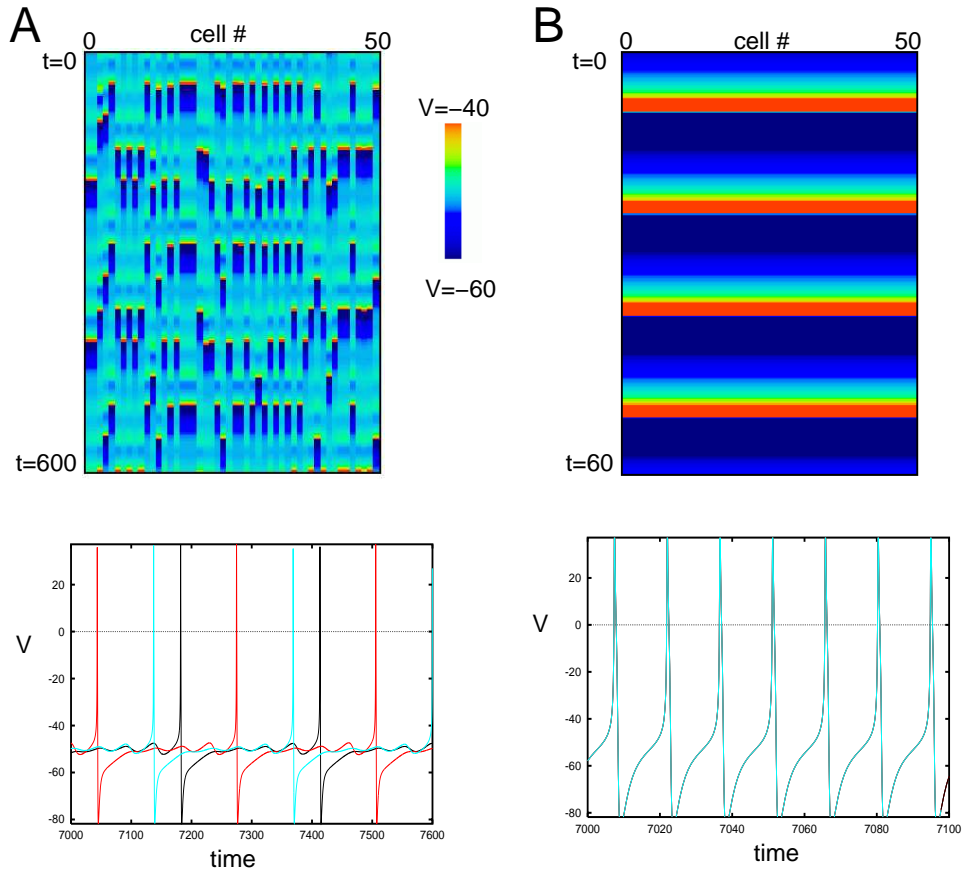
Fig. 2.5. *Clustering depends on the g_{Ks} and the subthreshold oscillations. (A) $g_{Ks} = 0.018$, $I_{app} = 0.675$, $g_{gap} = 0.0002$. As in figure 2.4, top shows voltage traces of all the cells and bottom shows representative voltages for cells in the clusters. (B) $g_{Ks} = 0$ shows synchronization.*

all-to-all coupling via gap junctions:

$$\begin{array}{rcll} C\,V_i' & = & I_{app} - (I_{Na} + I_K + I_{Ks} + I_L + I_{gap,i}), & i = 1, \ldots, N \\ x_i' & = & (x_{i,\infty}(V_i) - x_i)/\tau_{x_i}(V_i), & x_i = m_i, h_i, n_i, s_i, \end{array} \qquad (2.3)$$

where

$$I_{gap,i} = g_{gap} \frac{1}{N} \sum_{j=1}^{N} (V_i - V_j)$$

is the gap junction current cell i receives from all its $(N-1)$ neighbors j. All the other intrinsic ionic currents depend only on cell i itself. Additionally, to check for robustness, in some simulations, we add a small amount of independent Gaussian noise.

Figure 2.4 shows the result of a simulation of 50 cells coupled with $g_{gap} = 0.0002$ and $I_{app} = 0.7$. The cells organize themselves into three clusters of differing sizes. This structure is robust to a small amount of Gaussian noise (shown in B).

Figure 2.5 shows that STOs are necessary for the clustering to occur. In this figure, $I_{app} = 0.675$ and in the normal model there are three clusters as in Figure 2.4. However, if we remove g_{Ks}, the slow potassium channel, then the neurons robustly synchronize. Thus, the presence of the slow potassium current is needed for clustering to occur. If we maintain the slow potassium current, but increase the applied current into the regime where there is regular spiking (e.g, the red curves in Figure 2.1, say, $I_{app} = 1$), then the clustering disappears. If the coupling is strong enough, then clustering disappears leaving only synchrony. Thus, it seems that the clusters are a consequence of the interaction of subthreshold behavior with weak coupling. The remainder of the paper explores the mechanism for MMOs and how these impact the interactions for weak coupling.

3. Single cell analysis. In this section we want to uncover the mechanism that generates MMOs in the single cell Erisir model (2.1). In particular, we want to show that the generalized canard phenomenon [7, 49, 46, 39, 22, 50, 10] observed in slow/fast time-scales problems explains the STOs within MMO patterns. The current theory for MMOs via canards is developed for systems with 1 variable on the fast time-scale and 2 variables on the slow time-scale. Therefore, the analysis splits into the following parts: (a) identify 2 different time-scales in the Erisir model (Section 3.1); (b) perform a model reduction of the full 5D model to a 3D model with 1 fast and 2 slow variables (Section 3.2); (c) explain MMOs in the reduced problem via the generalized canard phenomenon (Sections 3.3–3.4).

3.1. Dimensionless version of Erisir model. A standard procedure to identify different (time-)scales in a biophysical model is to bring such a system into dimensionless form. Only in dimensionless form can one decide which parameters are small or large. We therefore rescale the dimensional variables V (dependent) and t (independent) with appropriate reference scales k_v and k_t:

$$V = k_v\, v\,, \qquad t = k_t\, \tau$$

where v and τ are the dimensionless versions of membrane voltage and time. Note that all the gating variables $x = m, h, n, s$ are dimensionless by definition. After rescaling we obtain the following dimensionless version of the Erisir model (2.1):

$$\begin{aligned} C/(g_{Na}k_t)\, v' &= \hat{I}_{app} - (\hat{I}_{Na} + \hat{I}_K + \hat{I}_{Ks} + \hat{I}_L)\,, \\ x' &= (k_t/\tau_x(v))(x_\infty(v) - x)\,, \qquad x = m, h, n, s\,, \end{aligned} \qquad (3.1)$$

with

$$\begin{aligned} \hat{I}_{Na} &= m^3 h(v - \hat{E}_{Na})\,, & \hat{I}_K &= \hat{g}_K\, n^2(v - \hat{E}_K)\,, \\ \hat{I}_{Ks} &= \hat{g}_{KS}\, s^4(v - \hat{E}_K)\,, & \hat{I}_L &= \hat{g}_L\,(v - \hat{E}_L)\,, \\ \hat{I}_{app} &= I_{appl}/(g_{Na}\, k_v) \end{aligned} \qquad (3.2)$$

and

$$\hat{g}_y = g_y/g_{Na}\,, \quad y = K, Ks, L\,, \qquad \hat{E}_z = E_z/k_v\,, \quad z = Na, K, L\,. \qquad (3.3)$$

If we look at the time traces in Figure 2.2 then we see that the membrane potential varies in the order of 100mV (maximum around 120mV) and we choose $k_v = 100\,mV$
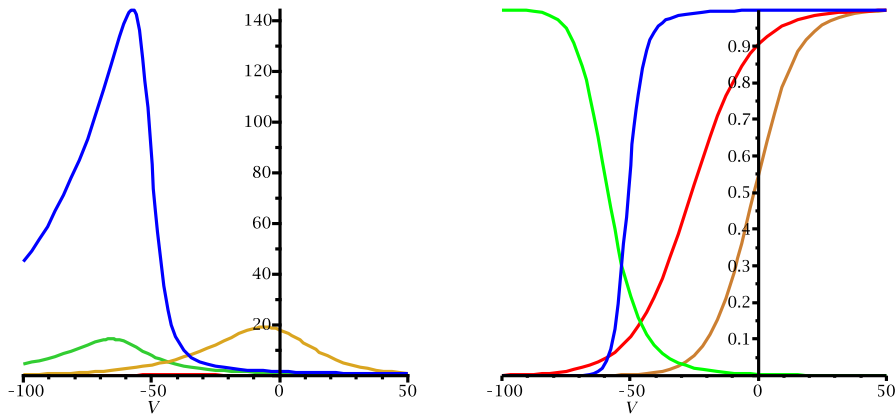
FIG. 3.1. *Voltage dependent time constants $\tau_x(V)$ (left) and voltage dependent quasi steady state $x_\infty(V)$ (right) of Erisir model (2.1): $\tau_m(V)$ and $m_\infty(V)$ (red); $\tau_h(V)$ and $h_\infty(V)$ (green), $\tau_n(V)$ and $n_\infty(V)$ (yellow), and $\tau_s(V)$ and $s_\infty(V)$ (blue). Note, $V = 100 \cdot v$ relates the voltage V to its dimensionless counterpart v. Similarly, $\tau_x(V)$ relates to $\tau_x(v)$ and $x_\infty(V)$ to $x_\infty(v)$.*

as a typical reference voltage scale[1]. Therefore, the right hand side of the voltage equation v in system (3.1) is basically of order one and the parameter $C/(g_{Na}) \approx 10^{-2}\,ms$ represents a typical time-scale of the voltage equation.

To identify the typical time-scales of the gates x we have to look at the voltage dependent time-scale functions $\tau_x(v)$ which are shown in Figure 3.1, left. We observe that the maxima of all the bell shaped functions are in the subthreshold regime $(V \leq -40\,mV)$ except for the gate n which has its maximum at $V \approx 0\,mV$. The bell shape curve indicates that typical time-scales vary depending on if the cell is in the subthreshold regime $(V \leq -40\,mV)$ or in the action potential regime $(V \geq -40\,mV)$. In the subthreshold regime typical time-scale orders are:

$$\tau_m \in \left(10^{-2}, 10^{-1}\right), \tau_h \in \left(10^0, 10^1\right), \tau_n \in \left(10^0, 10^1\right), \tau_s \in \left(10^1, 10^2\right),$$

while in the action potential regime typical time-scale orders are:

$$\tau_m \sim 10^{-2}, \tau_h \sim 10^0, \tau_n \in \left(10^0, 10^1\right), \tau_s \in \left(10^0, 10^1\right).$$

We have to choose the minimum order of each τ_x, $x = m, h, n, s$, to obtain the typical time-scale order of the gates. This suggests that m has a typical time-scale of order $10^{-2}\,ms$ while the other gates (h, n, s) are of order $1\,ms$. Alltogether, we have identified the different time-scales in system (3.1): a fast time-scale of order $10^{-2}\,ms$ for the fast variables (v, m) and a slow time-scale of order $1\,ms$ for the slow variables (n, h, s). We choose $k_t = 1\,ms$ as the (slow) reference time-scale and we obtain:

$$
\begin{aligned}
\varepsilon\, v' &= \hat{I}_{appl} - (\hat{I}_{Na} + \hat{I}_K + \hat{I}_{Ks} + \hat{I}_L)\,, \\
\varepsilon\, m' &= (1/t_m(v))(m_\infty(v) - m)\,, \\
h' &= (1/t_h(v))(h_\infty(v) - h)\,, \\
n' &= (1/t_n(v))(n_\infty(v) - n)\,, \\
s' &= (1/t_s(v))(s_\infty(v) - s)\,,
\end{aligned}
\tag{3.4}
$$

---

[1]In *dimensional analysis*, typical time-scales are found as combinations of the model parameters. Since we have a plethora of choices in this model we decided to make an empirical choice for easier comparison with the original model.
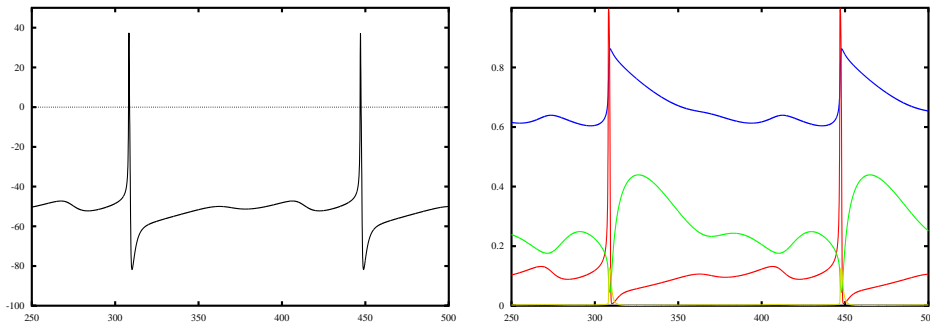
FIG. 3.2. *Time-traces in Erisir model for $I_{app} = 0.7$; Left: voltage time trace V shows MMO pattern 1^2; Right: corresponding time traces of gates - m (red); h (green), s (blue), n (yellow); Note that the n-gate is basically zero in the subthreshold regime.*

where $\varepsilon := C/(g_{Na}\, k_t) \approx 10^{-2} \ll 1$ is the singular perturbation parameter and the functions $t_x(v)$ are appropriate dimensionless versions of $\tau_x(v)$. System (3.4) is a slow/fast system with 2 fast variables (v, m) and 3 slow variables (h, n, s) on the slow time-scale τ ($' = d/d\tau$).

3.2. Reduction to a 3D model.

Step 1: Reduction of fast variables. In the literature it is a common procedure to reduce fast gating variables to their quasi steady state arguing that they reach these values very fast and the dynamics of these gates are of minor importance. In our case, we set the fast gating variable $m = m_\infty(v)$. This kind of reduction can be justified mathematically by a 'center manifold reduction'. We will not show this here but refer to [44] which showed such a reduction step rigorously for the m gate of the Hodgkin-Huxley model. With that first reduction step, we reduced the number of fast variables from two to one.

Step 2: Reduction of slow variables. This step is based on an observation in the subthreshold regime. Figure 3.2 shows a time-trace of the 'membrane potential' v (left) as well as the corresponding time-traces of the gates x, $x = m, h, n, s$, in system (3.4). Note that the n-gate does not influence the subthreshold regime at all, i.e. $n \approx 0$ in this regime. This can be easily explained by looking at the quasi steady state voltage functions $x_\infty(v)$ of the gates x shown in Figure 3.1. The sigmoidal activation function $n_\infty(v)$, the quasi steady state of n (shown in yellow), is approximately zero for $v < -0.4$ ($V < -40\, mV$), the limit of the subthreshold regime. The time constant $\tau_n(v)$ is of order $1\, ms$. Therefore, after an action potential is fired and the cell is repolarized to the subthreshold regime, n will reach its zero equilibrium value after a few milliseconds and n plays thereafter no role in the creation of STOs. Since we are primarily interested in the creation of the STOs in the MMO pattern it is reasonable to set $g_k = 0$, i.e. we block the Kv3.1 channel in the Erisir model. We expect to find qualitative similar results (MMOs) without this channel, but note that the Kv3.1 channel has a profound role in repolarizing the cell and we will come back to this point later.

With this second reduction step we reduced the number of slow variables from three to two.
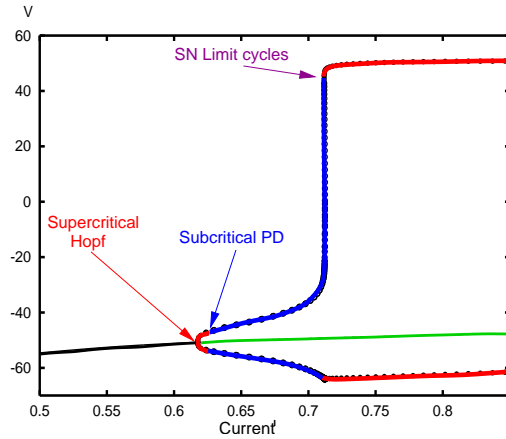
FIG. 3.3. *Bifurcation diagram of reduced Erisir model (3.5): for easier comparison with the original model (2.1) we use the applied current I_{app} as bifurcation parameter instead of its dimensionless counterpart $\hat{I}_{app}$. Similarly, we plot the phase variable V instead of its dimensionless counterpart v. We observe a supercritical Hopf bifurcation for $I_{app} \approx 0.62$, a limit cycle loses stability for $I_{app} \approx 0.63$ and we observe a saddle-node of limit cycles for $I_{app} \approx 0.71$.*

3.3. MMOs in the reduced Erisir model. In the following we will focus on the reduced Erisir model

$$
\begin{array}{rcl}
h' & = & (1/t_h(v))(h_\infty(v) - h) =: g_1(v, h) , \\
s' & = & (1/t_s(v))(s_\infty(v) - s) =: g_2(v, s) , \\
\varepsilon\, v' & = & \hat{I}_{appl} - (\hat{I}_{Na} + \hat{I}_K + \hat{I}_{Ks} + \hat{I}_L) =: f(v, h, s) ,
\end{array}
\tag{3.5}
$$

which is a singularly perturbed system (slow/fast system) with two slow variables (h, s) and one fast variable v. First we show that this model can produce similar patterns as the full Erisir model. Figure 3.3 shows the bifurcation diagram which has qualitatively the same structure as the bifurcation diagram of the full Erisir model shown in Figure 2.1: the cell is excitable for $I_{app} < I_{Hopf}$ where $I_{Hopf} \approx 0.615$ denotes a supercritical Hopf bifurcation. The corresponding limit cycle loses stability at $I_{app} \approx 0.625$ which opens a parameter window up to $I_{app} = I_{snlc} \approx 0.715$ with apparently no stable attractors. I_{snlc} denotes a saddle-node bifurcation of limit cycles. For $I_{app} > I_{snlc}$ there exist large relaxation type oscillations. Note that we use I_{app} and not its dimensionless counterpart $\hat{I}_{app}$ as bifurcation parameter. This allows us to compare the bifurcation structure directly with the bifurcation structure of the original model shown in Figure 2.1. Figure 3.4 shows time traces for several values of applied current I_{app}. Similar to the full Erisir model (2.1), MMOs show up as stable solutions for the reduced Erisir model filling the gap of apparently no stable solutions in Figure 3.3.

Note the qualitative differences between the full and the reduced Erisir model: the cell in the reduced Erisir model does not repolarize as much as in the full model (difference is approximately $15\,mV$). On the other hand, the cell depolarizes more in the reduced model than in the full model (difference is approximatelty $10\,mV$). This is explained by the Kv1.3 channel block which is responsible for the repolarization phase of the cell. Note that the gap between the HB and the SNLC in the bifurcation diagram of the reduced model, Figure 3.3, is just shifted slightly by $\Delta I_{app} \approx 0.03$ to
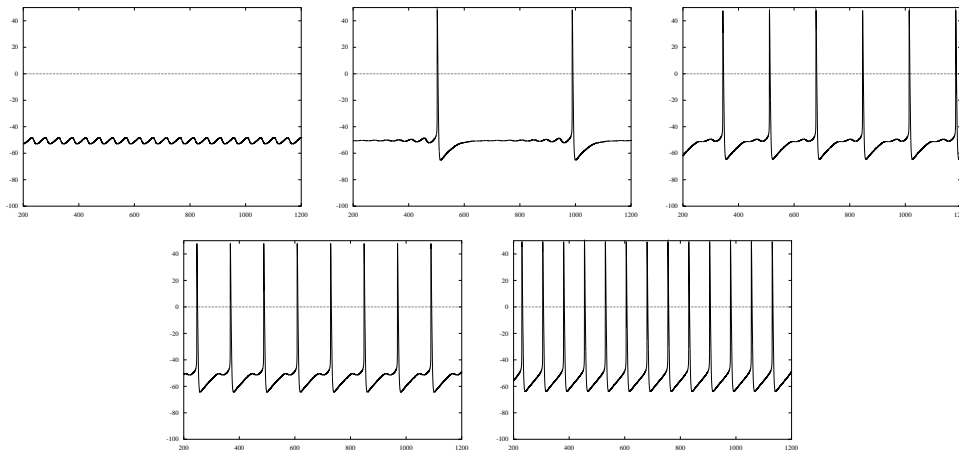
FIG. 3.4. *Voltage time traces of reduced Erisir model (3.5): Upper/Left: small oscillatory pattern 0^1 for $I_{app} = 0.62$; Upper/Middle: MMO pattern 1^9 for $I_{app} = 0.635$, Upper/Right: MMO pattern 1^2 for $I_{app} = 0.67$; Bottom/Left: MMO pattern 1^1 for $I_{app} = 0.69$; Bottom/Right: relaxation oscillation pattern 1^0 for $I_{app} = 0.72$. Note, we plot V instead of its dimensionless counterpart v.*

the left compared to the full model, Figure 2.1. This is (mainly) because the hyperpolarizing outward current I_K is very weak in the subthreshold regime (approximately zero) and has no influence on the STOs as explained in the reduction of the slow variables. In summary, it appears that the reduced Erisir model (3.5) covers qualitatively the behaviour of the full Erisir model (2.1), at least close to the parameter regime where we observe MMOs.

3.4. Canard analysis of reduced Erisir model. Here we explain the observed MMOs via the generalized canard phenomenon [7, 44, 49]. The canard theory applies to singular perturbation problems with two slow and one fast variables. The reduced Erisir model (3.5) has to fulfill a set of assumptions such that this theory can be applied, which we will show in the following.

We first focus on the limiting problem $\varepsilon \to 0$ in system (3.5) which is called the *reduced problem*. It describes the evolution of the slow variables (h, s) on the *critical manifold* $S := \{(v, s, h) \in \mathbb{R}^3 : f(v, s, h) = 0\}$, i.e., on the v-nullsurface. This critical manifold S can be represented as a graph over, e.g., (s, v)-space given by

$$h(s, v) = \frac{\hat{I}_{app} - \hat{g}_{ks}s^4(v - \hat{E}_k) - \hat{g}_L(v - \hat{E}_L)}{m_\infty^3(v)(v - \hat{E}_{Na})} \ . \tag{3.6}$$

The following assumption on the critical manifold S holds:

ASSUMPTION 1. *System (3.5) possesses (locally) in the subthreshold regime a folded critical manifold.*

Figure 3.5 (middle) shows the critical manifold for $I_{app} = 0.65$ and it is indeed folded. This is true for all I_{app} parameter values within the observed MMO regime (and beyond).

If we rescale to the fast time $\tau = t/\varepsilon$ in system (3.5) and take the singular limit $\varepsilon \to 0$, then we obtain the one-dimensional *layer problem* which describes the fast dynamics away from the critical manifold S. Trajectories of the layer problem evolve
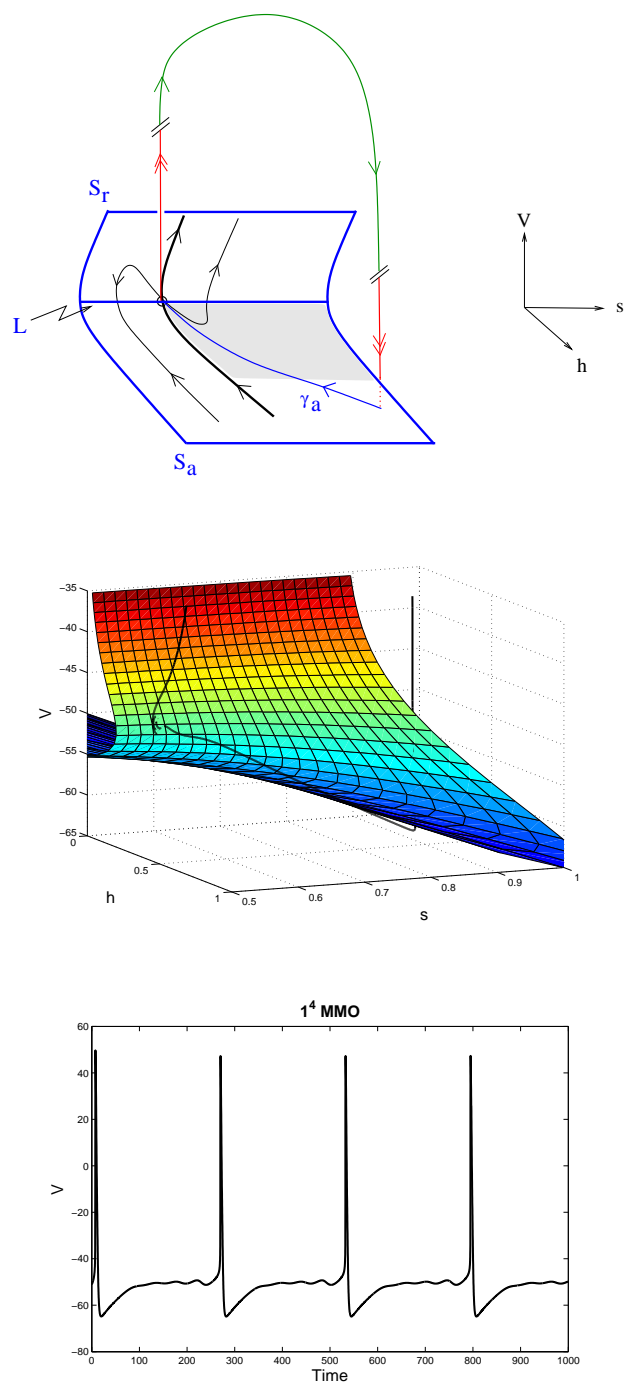
FIG. 3.5. *Explanation of MMOs via generalized canard phenomenon: the upper figure shows a sketch of a singular periodic orbit in phase space which predicts MMOs; the middle figure shows the critical manifold and a trajectory of system (3.5) with 4 STOs in the phase space near the corresponding folded node singularity; the lower figure shows the corresponding time trace of the 1^4 MMO pattern for $I_{app} = 0.65$. Note, we plot V instead of its dimensionless counterpart v.*

along fast fibers, i.e. one dimensional sets $(h = const, s = const, v)$, and the critical manifold S is a manifold of equilibria. The folded structure of S implies saddle-node bifurcations of equilibria within the layer problem along the fold-curve L. Therefore, we can describe the critical manifold as the union of subsets $S = S_a \cup L \cup S_r$ where S_a denotes the attracting (stable) branch of S, i.e. $f_v < 0$ on S_a, and S_r denotes the repelling branch of S, i.e. $f_v > 0$ on S_r. The fold-curve L is defined by $f_v = 0$. Therefore, the layer flow is towards S_a respectively away from S_r along fast fibers.

To understand the reduced flow on the critical manifold S, we project the limiting system $\varepsilon \to 0$ of (3.5) onto (s, v)-space. This projection can be obtained from implicit differentiation of $f(h, s, v) = 0$ and the equation for $\dot{s}$ which gives

$$\begin{aligned} \dot{s} &= g_2 \\ -f_v \dot{v} &= f_h g_1 + f_s g_2 \end{aligned} \tag{3.7}$$

evaluated along $h = h(s, v)$. Note that this is a natural choice for projection since S is given as a graph over (s, v)-space in (3.6). System (3.7) is singular along the fold-curve L given by $f_v = 0$. We therefore rescale time by the factor $-f_v$ to obtain the *desingularized reduced flow*

$$\begin{aligned} s' &= -f_v g_2 \\ v' &= f_h g_1 + f_s g_2 \end{aligned} \tag{3.8}$$

where 'prime' denotes differentation with respect to the new time $t_1 = t/(-f_v)$. We obtain the phase portait of the reduced system (3.7) by reversing the orientation of the trajectories of the desingularized system (3.8) on the repelling branch S_r, otherwise the two phase portraits are equivalent. System (3.8) has two types of singularities, regular and folded. Regular singularities are given by $g_1 = g_2 = 0$. They correspond to equilibria of the reduced flow (3.7) away from the fold-curve. In contrast, folded singularities are given by $f_v = 0$ (the fold-curve condition) and $f_h g_1 + f_s g_2 = 0$ which defines isolated points on the fold-curve. In general, such folded singularities are not equilibria of the reduced system (3.7). However, folded singularities give the opportunity for the reduced flow to cross from S_a to S_r via folded singularities in finite time. Depending on the classification as singularities of (3.8), folded singularities are called folded saddles, folded saddle-nodes, folded nodes or folded foci.

ASSUMPTION 2. *System (3.7) possesses a folded node (folded saddle-node) singularity for $0.55 < I_{app} < 0.74$.*

Figure 3.6 shows the reduced flow in the silent phase $(V < -40mV)$ for several values of applied current I_{app}. The lower orange curve represents the fold-curve L of the critical manifold. For $I_{app} < 0.55$, there exists a node on the attracting branch S_a and a folded saddle (not shown). For $I_{app} = I_{fsnII} \approx 0.55$, we observe a folded saddle-node (type II), the intersection of the green nullcline and the lower orange fold-curve, and a folded saddle, another intersection of the green nullcline and lower orange fold-curve (can be seen in e.g. Figure 3.6, $I_{app} = 0.63$). For $I_{app} > I_{fsnII}$, the folded saddle-node (type II) splits then into a folded node and a saddle (see e.g. Figure 3.6, $I_{app} = 0.63$). Therefore, a folded saddle-node (type II) corresponds to a transcritical bifurcation of a folded and a regular singularity. For $I_{app} = I_{fsnI} \approx 0.74$ we observe another folded saddle-node (type I) bifurcation, i.e. the folded node (left) and the folded saddle (right) annihilate each other (transition in Figure 3.6 from $I_{app} = 0.73$ to $I_{app} = 0.80$). Therefore, a folded saddle-node (type I) is a saddle-node bifurcation of folded singularities which explains the difference between the two sub-types. For
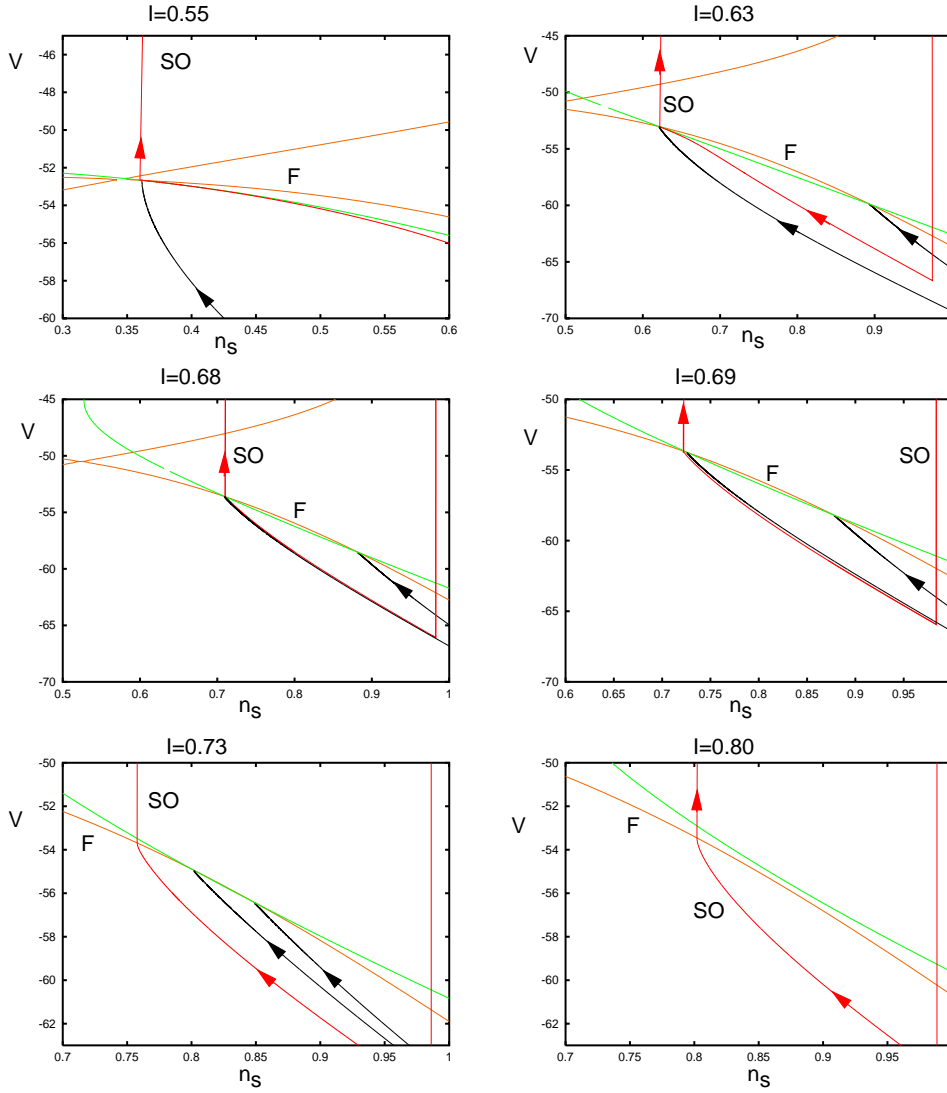
FIG. 3.6. *The reduced flow (3.7) of system (3.5). Note, we plot V instead of its dimensionless counterpart v. Applied current I_{app} is shown above each panel. Red curves are the singular orbit (SO; computed by solving system (3.5) with $C = 10^{-8}$, equivalent to very small $\epsilon \approx 10^{-8}$); green curve is the V-nullcline; orange curves are the n_s-nullclines (note the lower part, the fold-curve labeled F defined by $f_v = 0$, is not a true nullcline but its intersections with the green curve determine the folded nodes). Black curves (either alone or leftmost) represent the primary strong canard and rightmost black curves are the stable manifolds of the folded saddle. The sector on S_a (below the fold-curve F) bounded by the two black curves (the strong canard of the folded node and the canard of the folded saddle) is called the* funnel. *When the SO lies within the funnel, there will be MMOs for sufficiently small values of ϵ according to the theorem.*

$I_{app} > I_{fsnI}$ there just exists the ordinary saddle on the repelling branch S_r (the intersection of the green curve with the upper orange curve, not shown). Hence, Assumption 2 is fulfilled for $I_{fsnII} < I_{app} < I_{fsnI}$ as stated.

Note that a folded node creates a *singular funnel* on S_a, i.e. there exists a sector of solutions of the reduced flow (3.7) which is 'funneled' from S_a through the folded
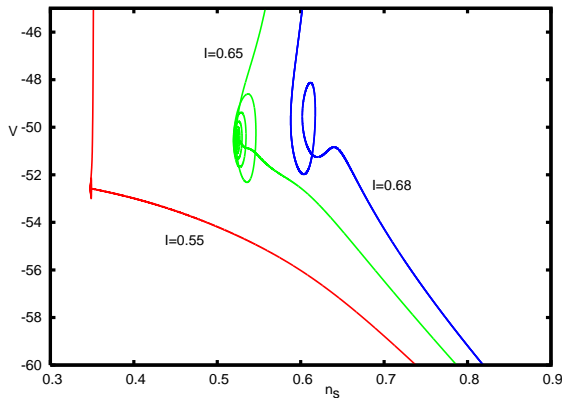
FIG. 3.7. *Trajectories of system (3.5) projected onto (n_s, V) plane at different currents corresponding to Figure 3.6*

node to S_r. In Figure 3.6, the singular funnel is the area between the fold curve (lower orange curve) and the two black curves, the primary strong canard of the folded node and the canard of the folded saddle. Identifying this funnel region is essential since solutions of system (3.5) which pass through this funnel region will create STOs. Finally, we have to construct singular periodic orbits, concatenated by trajectory segments of both the reduced and the layer problem which explain the observed MMO patterns in (3.5).

ASSUMPTION 3. *System (3.5) possesses for $0.55 < I_{app} < 0.69$ a singular periodic orbit which consists of a segment on the stable folded surface S_a within the singular funnel of the folded node singularity as an endpoint.*

Such a singular periodic orbit (SO) is illustrated in Figure 3.5. The main step to find these SOs is to show that the return mechanism projects the fast fiber of the folded node back into the funnel region (see Figure 3.5). We do not calculate this singular periodic orbits explicitly, but approximate them by calculating periodic orbits in system (3.5) with very small $\varepsilon \approx 10^{-8}$. In the singular limit $\varepsilon \to 0$ these periodic orbits will become the singular periodic orbits described in Assumption 3. Several examples of SOs are shown in Figure 3.6. The funnel of the folded node becomes obviously smaller with increasing I_{app} and disappears for $I_{app} = I_{fsnI}$ (the folded saddle-node type I). The global return mechanism projects the fast fiber of the folded node only for $0.55 < I_{app} < I_{rel} \approx 0.69$ into the funnel as shown in Figure 3.6. Therefore, Assumption 3 is only fulfilled for $I_{fsnII} < I_{app} < I_{rel}$. For $I_{app} \approx 0.68$ the return mechanism projects onto the border of the funnel, the strong canard of the folded node which represents the separatrix in the phase space for different oscillatory behaviour, i.e. between MMOs and relaxation oscillations. It was shown in [7] that if a singularly perturbed system fulfills Assumptions 1-3 then it possesses 1^s MMO patterns for sufficiently small ε. We conclude:

PROPOSITION 3.1. *System (3.5) possesses MMO type periodic solutions based on the canard phenomenon for sufficiently small $\varepsilon \ll 1$.*

Note that by Assumptions 2 and 3 we expect to find MMOs for $I_{fsnII} \approx 0.55 < I_{app} < I_{rel} \approx 0.69$. Obviously, the boundaries of this prediction are sensitive to the size of the singular perturbation parameter $\varepsilon \ll 1$. For example, the bifurcation

diagram of system (3.5), Figure 3.3, is calculated for $\varepsilon \approx 10^{-2}$. We observe MMO patterns for $I_{Hopf} \approx 0.615 < I_{app} < I_{snlc} \approx 0.715$. There is a marked shift in the onset of MMOs compared to the prediction $I_{fsnII} = 0.55$. If we decrease the value of ε towards zero then I_{Hopf} converges to I_{fsnII}, i.e. a folded saddle-node (type II) is the singular limit representation of the Hopf bifurcation shown in Figure 3.3. Note further that a stable node on S_a crosses the fold-curve L at I_{fsnII} to become a (unstable) saddle on S_r. These equilibria (saddle and node) persist under small pertubations ε and are therefore also equilibria of (3.5). Recall the transcritical bifurcation of a folded and an ordinary singularity at $I_{fsnII} \approx 0.55$. These stable and unstable equilibria correspond to the branch of equilibria in the bifurcation diagram, Figure 3.3, where stability is lost via a Hopf bifurcation. This again emphasizes the relation between the folded saddle-node (type II) and the Hopf bifurcation. The smaller the singular perturbation ε, the closer the onset of MMOs to $I_{fsnII} \approx 0.55$.

To obtain MMO patterns it is essential that Assumption 3 is fulfilled as well. The return mechanism has to project within the funnel, otherwise we will only observe relaxation oscillations but not MMOs. Therefore, the global return mechanism ultimately determines the I_{app} interval where MMOs are observed. In Figure 3.3, the upper limit I_{snlc} is the parameter value where the return mechanism of system (3.5) with $\varepsilon \approx 10^{-2}$ projects onto the border of the funnel. Again, if we decrease ε towards zero then I_{snlc} approaches I_{rel} as predicted by the singular limit theory. Note that ε has an increasing effect on the MMO range at the upper limit I_{snlc} while it has a decreasing effect on the MMO range at the lower limit I_{Hopf}.

We can also give a qualitative prediction on the number of STOs within the MMO pattern, the larger I_{app} the smaller the number of STOs. Canard theory [49] predicts an upper limit on the number of STOs, $s^* = [(\mu + 1)/(2\mu)]$ (the largest integer less than or equal $(\mu + 1)/(2\mu)$), based on the eigenvalue ratio $\mu = \lambda_1/\lambda_2 < 1$ of the folded node singularity in system (3.8). This number decreases with increasing applied current[2] for $I_{fsnII} \approx 0.55 < I_{app} < I_{rel} \approx 0.69$. Furthermore, the return mechanism projects the trajectory closer to the strong canard for increased I_{app}. The number of STOs is smaller than the predicted maximal number s^* whenever the return mechanism projects the trajectory $O(\varepsilon^{(1-\mu)/2})$ close to the strong canard. In the limit $I_{app} = I_{rel}$, i.e. the switch from MMOs to relaxation oscillations, the number s^* of STOs becomes zero. This explains the decreased number of STOs within an MMO pattern for increased I_{app} shown in Figure 3.4 and Figure 3.7.

We want to point out that the canard theory developed in [7, 49] cannot fully explain the transition from STOs to MMOs near a folded saddle-node ($I_{app} = I_{fsnII}$). Note that the limit $\mu \to 0$ predicts infinitely many STOs, i.e. a transition from STOs to MMOs. As pointed out in our analysis, the onset of STOs is associated with a Hopf bifurcation which in the singular limit corresponds to a folded saddle-node (type II). In [35], a rigorous blow-up analysis of a folded saddle-node type II singularity is presented which shows how two phenomena, canards and a singular Hopf bifurcation, lead to complicated dynamics including STOs and MMOs. In [25], it is shown how one determines the type of the Hopf bifurcation associated with a folded saddle-node type II singularity (super– or subcritical). It also shows numerical results on nearby bifurcation structures such as period doubling and torus bifurcation. Other work on folded saddle-nodes can be found in [39, 34].

---

[2]The eigenvalue ratio $\mu = \lambda_1/\lambda_2 < 1$ is not a monotone function of I_{app}. The value μ reaches its maximum ($\hat{\mu} \approx 0.27$) for $0.69 < I_{\hat{\mu}} < 0.7$. It increases from zero to $\hat{\mu}$ for $I_{fsnII} < I_{app} < I_{\hat{\mu}}$ and decreases from $\hat{\mu}$ to zero for $I_{\hat{\mu}} < I_{app} < I_{fsnI}$.

4. Weak coupling of the Erisir model. We now use weak coupling theory [14] to try to understand how the presense of the canards produces the ability of networks to form clusters. Briefly, weak coupling theory or averaging allows one to reduce systems of N coupled oscillators to sets of differential equations on an $N-$torus. Consider a coupled pair:

$$X_1' = F(X_1) + \epsilon_1 G_1(X_1, X_2)$$
$$X_2' = F(X_2) + \epsilon_1 G_2(X_1, X_2)$$

where $X' = F(X)$ has a stable limit cycle $U(t)$ and ϵ_1 is small and positive. Here ϵ_1 is used to denote the coupling strength with the subscript 1 to distinguish it from the ϵ used to characterize the difference in time-scales in the previous section. In order for averaging and weak coupling theory to be applied, one generally has to assume that $\epsilon_1 \ll \epsilon$. That is the coupling is "smaller" than any of the other rates characterizing the uncoupled dynamics. If this assumption holds, then the method of weak coupling allows us to conclude that for ϵ_1 sufficiently small, $X_j(t) = U(\theta_j(t)) + O(\epsilon_1)$ and

$$\theta_1 = 1 + \epsilon_1 H_1(\theta_2 - \theta_1) + o(\epsilon_1)$$
$$\theta_2 = 1 + \epsilon_1 H_2(\theta_1 - \theta_2) + o(\epsilon_1)$$

where

$$H_j(\phi) = \frac{1}{T} \int_0^T U^*(t) \cdot G_j(U(t), U(t + \phi)) \, dt.$$

Here T is the period of the limit cycle and $U^*(t)$ is the unique periodic solution to the linear adjoint problem:

$$Y' = -D_X F(U(t))^T Y, \qquad Y(t) \cdot U'(t) = 1.$$

For our model, coupling is only through the voltage of the membrane, so that

$$H(\phi) = \frac{1}{T} \int_0^T V^*(t)(V(t + \phi) - V(t)) \, dt. \tag{4.1}$$

$V^*(t)$ is the voltage component of the adjoint and is proportional to the phase-resetting curve obtained by applying brief small current perturbations to the neuron (see [29]). $V(t)$ is the voltage trace. We note that for gap junctions, $H(0) = 0$. Phase models enable us to predict the possible stable phase-locked patterns when two or more oscillators are coupled. For a pair of identical oscillators, we can write a single scalar equation for the phase-difference, $\phi := \theta_2 - \theta_1$:

$$\phi' = \epsilon_1[H(-\phi) - H(\phi)] = -2\epsilon_1 H_{odd}(\phi).$$

Thus, the zeros of the odd part of H are the possible phase-differences and a phase difference of $\bar{\phi}$ is stable if $H'(\bar{\phi}) > 0$.

The generalization of the above theory to N oscillators is clear. In particular, for all:all coupling with identical oscillators, we obtain the following model for the phases:

$$\theta_i' = 1 + \epsilon_1 \frac{1}{N} \sum_{j=1}^N H(\theta_j - \theta_i). \tag{4.2}$$

A clustered solution for this system is a partition of N, that is a collection of positive integers whose sum is N, say, $k_1, \ldots, k_m$ such that there are m distinct phases and k_l oscillators which are all synchronized in each group. For example, a two-cluster solution would have n oscillators with 0 relative phase and $N - n$ oscillators with $\bar{\phi}$ relative phase. The existence of $m-$clustered states requires solving m equations. Stability of these clustered states is far more difficult to determine and has been done in general only for the $m = 2$ case and for $m > 2$ for certain symmetric cases [28, 26, 1].

For very large N, one technique that is very useful was developed by Kuramoto [36]. He considers globally connected identical oscillators which are driven by uncorrelated noise. For large enough noise, the density of the phases for the noisy system as $N \to \infty$ is uniform (the asynchronous state). He performs a stability analysis on this state as the amplitude of the noise decreases and under some conditions, the asynchronous state loses stability to a symmetric clustered state. Which state emerges from the noise is very easy to determine. Let a_n denote the Fourier sine coefficients of $H(\phi)$. Then an m-cluster will bifurcate from the asynchronous state when the noise falls below a_m/m. Thus, we need only look at the biggest a_m/m to predict which clusters should emerge, as the noise is reduced. While this will not pick out all the attractors, we can think of it as the analogue of simulated annealing in the hopes that the most attractive state is chosen.

Thus, in the remainder of this section, we will look at the H function for the Erisir model and then try to understand why it looks like it does by considering the subthreshold behavior.

4.1. Phase models for the Erisir model. Using the theory outlined above, the main determinant of the behavior is the function $H(\phi)$ which gives (i) the possible stable pairwise phase-differences and (ii) the form of the most stable cluster formation in the presence of noise.

Figure 4.1 shows the behavior of a phase model of the form (4.2) where H is as defined in equation (4.1) for the Erisir model with different values of I_{app}. The initial phase are randomly taken from a uniform distribution. In the leftmost panel, the phases organize into a three cluster solution as in the full model shown in Figure 2.4, $I_{app} = 0.7$. The two graphs below show the interaction function H along with the adjoint, V^*. It is clear that H contains many higher order Fourier modes and, in fact, the maximum of a_m/m occurs at $m = 3$, so that the three cluster solution is predicted to be the most stable one. As the current is increased and the system moves closer to the usual repetitive firing regime, the number of clusters drops to two ($I_{app} = 0.8$) and then to one ($I_{app} = 0.9$) which is the synchronous solution. The Fourier analysis of H for $I_{app} = 0.8$ shows that $a_2/2$ is maximal so that two-clusters are predicted to emerge from the asynchronous solution. Similarly, the dominant Fourier sine model is $m = 1$ for $I_{app} = 0.9$ so that there will only be synchrony.

We note that for the three cluster case, that H is close to the mirror image of V^*. The reason for this can be seen by looking at the definition of H, (4.1). The H function is the convolution of the voltage trace with the adjoint. However, for the long-periodic oscillations associated with clustering, the voltage trace looks very close to a Dirac delta function, so that a rough approximation of H is

$$H(\phi) \approx \frac{1}{T} \int_0^T V^*(t)[\delta(t + \phi) - \delta(t)] \, dt = V^*(-\phi) - V^*(0) \qquad (4.3)$$

which is just the mirror image of $V^*(t)$. This suggests that the key to understanding clustering lies in the adjoint (PRC) rather than the voltage trace. This notion is
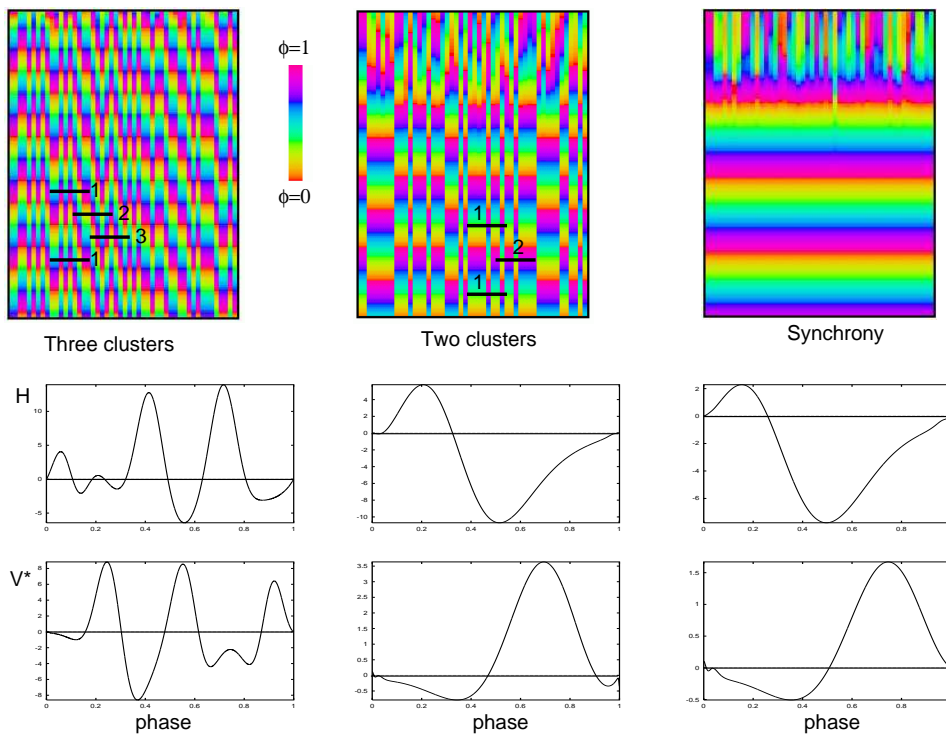
FIG. 4.1. *Behavior of the phase-reduction of the Erisir model for 50 coupled oscillators. Each column shows the phases of each oscillator with time running downward and oscillator index across. The function $H(\phi)$ is then shown and the adjoint, $V^*(\phi)$ is at the bottom. Applied current I_{app} from left to right is 0.7, 0.8, and 0.9 $\mu A/cm^2$. Fourier analysis of H predicts three, two, and one cluster solutions respectively.*

borne out by looking at Figure 4.2, in which we use the shape of the adjoint for $I_{app} = 0.675$ (many subthreshold oscillations in V and many oscillations in $V^*(t)$) and for the same current but with g_{Ks} turned off (no subthreshold oscillations and a simple bimodal $V^*(t)$.) We compute four different versions of H using all combinations of the complex/simple adjoint and the complex/simple voltage trace. As the figure illustrates in curves 1 and 2, the complex adjoint combined with either of the two voltage traces leads to a highly oscillatory function H while the simple adjoint yields relatively simple functions H. Thus, the numerics here and the approximation (4.3) provide strong evidence that the multiple oscillations in the interaction function, H are due to the complexity of the adjnt/PRC, $V^*(t)$ and not to the waveform of the membrane potential.

If we recall that the adjoint is very closely related to the phase response curve (PRC), then we can exploit this to understand the role of the canard structure and subthreshold oscillations in shaping the PRC. Figure 4.3 shows a blowup of the sub-threshold region in the $V - n_s$ phase plane. The unperturbed period is 234 msec. Two different brief (0.1 msec) pulses are delivered at either 70 msec or 90 msec after the neuron spikes. The 70 msec pulse results in a delay of the next spike by 45 msec while the 70 msec pulses causes the spike to occur 42 msec earlier. The mechanism for this difference is clear from the figure. The earlier pulse makes the neuron undergo an additional oscillation (red loop in the center) while the later pulse causes the neuron
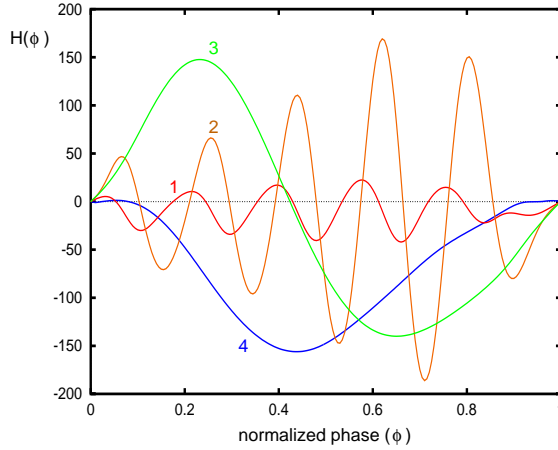
FIG. 4.2. *The adjoint is responsible for the shape of H. Four curves show H computed with the standard model ($I_{app} = 0.657, g_{Ks} = 0.018$) or the simpler model, ($I_{app} = 0.675, g_{Ks} = 0$). 1: standard voltage trace + standard adjoint; 2: simpler voltage trace + standard adjoint; 3: simple voltage trace + simple adjoint; 4: standard voltage trace + simple adjoint.*
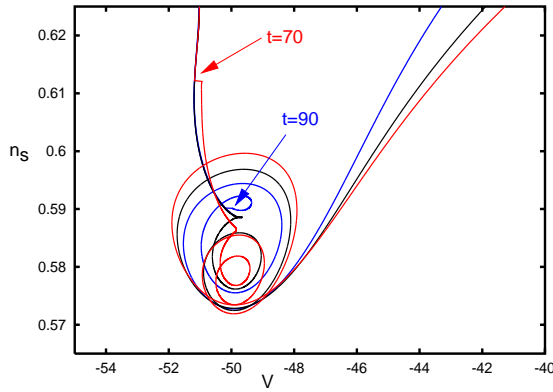

FIG. 4.3. *Explanation for the complexity of the PRC (adjoint). Small differences in the timing of brief input have magnified effects near the subthreshold dynamics. Here ($I_{app} = 0.675$ and the period is about 234 msec. A current pulse lasting 0.1 msec with amplitude 0.25 $\mu A/cm^2$ is delivered at $t = 70$ (red curve) and $t = 90$ (blue curve msec after the spike. Black curve is unperturbed trajectory.*

to skip a pulse. Thus, the presence of the subthreshold oscillations leads to sensitivity to the timing of small pulses and a PRC which has multiple advances and delays during the cycle.

Finally, we note that the same behavior is found in the reduced (three-variable model). Figure 4.4 shows the adjoint and the interaction function for the reduced model when $I_{app} = 0.65$ which is in the region where there is a folded canard structure. Compare this adjoint/H function with that in Figure 4.1 on the left. They are clearly quite close in qualitatve shape. Thus, the reduction has little effect on the phase dynamics.
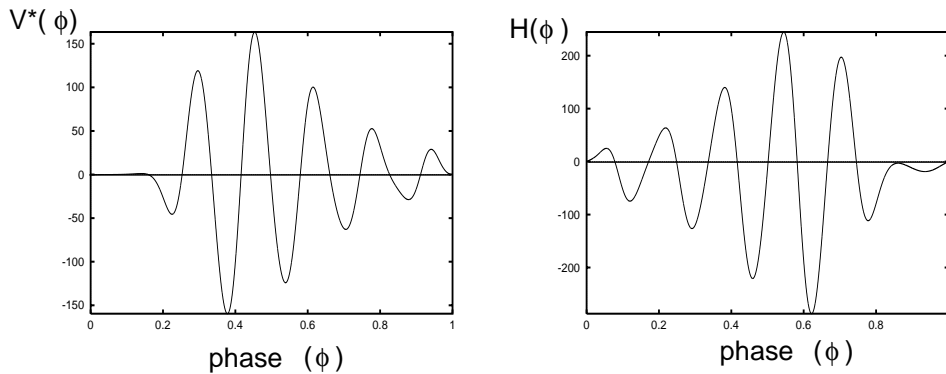
FIG. 4.4. *The adjoint, $V^*(\phi)$ and the interaction function, $H(\phi)$ for the reduced Erisir model with $I_{app} = 0.65$ which is in the regime where there is a folded canard. Compare these to the corresponding functions for the full model in the left panel of figure 4.1.*

5. Conclusion. In this paper, we have explored the interactions between local dynamics and coupling of neural oscillators. Our choice of coupling, electrical, is motivated by the preponderance of such connections between inhibitory interneurons in the brain (particularly, the cortex). Electrical coupling is also the simplest form of coupling and does not introduce the additional complexities of synaptic coupling which involve a variety of time-scales and the kinds of synapses (inhibitory or excitatory). The model used in the present paper has been used by other authors in order to study the synchronization properties of inhibitory neurons. The novel aspect of the biophysical model is that it contains a slow potassium channel which enables the voltage to undergo mixed-mode oscillations (MMOs). This mixture of spikes and subthreshold oscillations makes the neuron very sensitive to inputs and leads to a complex phase-resetting curve (PRC). This complex PRC provides the mechanism for multiple clustering in networks of these neurons. There have been few other studies of the interactions between MMOs and coupling. [2] found clustering with strong coupling in a chemical model. In their paper, the main tools were fast slow analysis; weak coupling and phase methods were not applied. [30] looks at weak coupling between elliptic bursters (which are related to MMOs, cf [12]). He is only interested in spike versus burst synchrony and does not relate the dynamics to the interaction function.

Biologically, this work provides a novel contribution to the analysis of the effects of slow currents on dynamics and coupling. There have been a number of papers which show that slow currents and other intrinsic currents have profound effects on synchronization [41, 27, 16, 21], however, all these illustrated transitions between synchrony and "anti-phase" oscillations. Furthermore, while the effects were often shown to be a consequence of changing the shape of the PRC, these shape changes were subtle. In the present paper, the slow potassium current I_{Ks} has a profound effect and produces MMOs which, in turn, result in a very complex PRC. Rotstein et al. [43] identified a slow h-current I_h in an entorhinal cortex layer II stellate cell model mainly responsible for observed MMOs and showed that the canard phenomenon explains these MMOs as well. They also pointed out the effect of MMOs on the PRC.

Strong coupling destroys the clustering ability of these networks (results not shown) and this can be understood by also noting that strong pulses do not have the same subtle effects on the PRC as do weak pulses. Thus, the results described

here require "weak" coupling. We point out that the coupling conductance is about 10% of the slow potassium conductance. Finally, we remark that similar results are found with weak inhibitory synaptic coupling as long as the synapse are short-lasting.

Appendix A. Functions and parameters of Erisir model (2.1).
The biophysical model has the form:

$$C\,V' = I_{app} - g_L(V - E_L) - g_{Na}m^3h(V - E_{Na}) - g_K n^2(V - E_K) - g_{Ks}s^4(V - e_K)$$
$$m' = a_m(V)(1 - m) - b_m(V)m$$
$$h' = a_h(V)(1 - h) - b_h(V)h$$
$$n' = a_n(V)(1 - n) - b_n(V)n$$
$$s' = a_s(V)(1 - s) - b_s(V)s.$$

where:

$$a_m(V) = 40(75 - V)/(\exp((75 - V)/13.5) - 1)$$
$$b_m(V) = 1.2262\exp(-V/42.248)$$
$$a_h(V) = 0.0035\exp(-V/24.186)$$
$$b_h(V) = 0.017(-51.25 - V)/(\exp(-(51.25 + V)/5.2) - 1)$$
$$a_n(V) = (95 - V)/(\exp((95 - V)/11.8) - 1)$$
$$b_n(V) = 0.025\exp(-V/22.22)$$
$$a_s(V) = -(0.616 + 0.014V)/(\exp(-(44 + V)/2.3) - 1)$$
$$b_s(V) = 0.0043\exp(-(44 + V)/34)$$

The kinetics of these variables are exactly as published in [38]. We have made some small changes to the conductances (in particular, our leak, g_L is somewhat larger). The current I_{app} is varied as is the slow conductance, g_{KS}. Unless otherwise indicated, the default values are $E_K = -97$, $E_{Na} = 55$, $E_L = -70$ (all in mV), $C = 0.1\mu F/cm^2$, $g_L = 0.041, g_K = 18, g_{Na} = 9$ and $g_{Ks} = 0.018$ (all in $\mu S/cm^2$).

In the network model, 50 such cells are coupled together via global coupling:

$$I_{coup} = \frac{g_{gap}}{50}\sum_{j=1}^{50}(V_j - V_i)$$

which is added to the right-hand side of the voltage equation for each oscillator. In simulations with noise, a normally distributed random variable is added to each voltage equation.

REFERENCES

[1] Ashwin P, Swift JW. The dynamics of n weakly coupled oscillators. J. Nonlinear Sci., 2:69–108, 1992.
[2] Baba, N and Krischer, K Mixed-mode oscillations and cluster patterns in an electrochemical relaxation oscillator under galvanostatic control Chaos 18, 015103 (2008) (9 pages)
[3] Banaji M. Clustering in globally coupled oscillators. Dynamical Systems, 17(3):263–285, 2002.
[4] Benoıt E (1983), *Systèmes lents-rapides dans R^3 et leur canards*, Astérisque **109-110**:159-191.

[5] Bold K., Edwards C., Guckenheimer J., Guharay S., Hoffman K., Hubbard J. Oliva R., Weckesser W. (2003), SIAM J Appl. Dyn. Syst. 2, 570-608.

[6] Brøns M., Kaper T., Rotstein H. (2008), Introduction to Focus Issue: Mixed Mode Oscillations: Experiment, Computation, and Analysis Chaos 18, 015101.

[7] Brøns M., Krupa M., Wechselberger M., Mixed Mode Oscillations Due to the Generalized Canard Phenomenon, Fields Institute Communications (2006), Vol. 49, 39-63.

[8] Brown E., Holmes P., Moehlis J. Globally coupled oscillator networks. In E. Kaplan, J. Marsden, and K. Sreenivasan, editors, Perspectives and problems in Nonlinear Science: A celebratory Volume in Honor of Larry Sirovich, pages 183–215. Springer, New York, NY, 2003.

[9] Chow CC, Kopell N (2000) Dynamics of spiking neurons with electrical coupling. Neural Comp 12:1643-1678.

[10] Desroches M., Krauskopf B., Osinga H. (2008) The geometry of slow manifolds near a folded node, preprint.

[11] Doi S, Inoue J, Kumagai S (2004), *Chaotic spiking in the Hodgkin Huxley nerve model with slow inactivation of the sodium current*, J Integr Neurosci, **3**:207-225.

[12] Drover, J., Rubin, J., Su, J. and Ermentrout, B., Analysis of a canard mechanism by which excitatory synaptic coupling can synchronize neurons at low firing frequencies, SIAM J. Appl. Math., 65 (2004), pp. 69-92.

[13] Erisir A, Lau D, Rudy B, Leonard S (1999) Function of specific K+ channels in sustained high-frequency firing of fast-spiking neocortical cells. J Neurophysiol 82:2476-2489.

[14] Ermentrout, GB and Kopell N (1984) Frequency Plateaus in a Chain of Weakly Coupled Oscillators, I. SIMA 15:215-237.

[15] Ermentrout B. Gap junctions destroy persistent states in excitatory networks. Phys Rev E Stat Nonlin Soft Matter Phys. 2006 Sep;74(3 Pt 1):031918. Epub 2006 Sep 27.

[16] Ermentrout B, Pascal M, Gutkin B. The effects of spike frequency adaptation and negative feedback on the synchronization of neural oscillators. Neural Comput. 2001 Jun;13(6):1285-310.

[17] Gao J, Holmes P. On the dynamics of electrically-coupled neurons with inhibitory synapses. J Comput Neurosci. 2007 Feb;22(1):39-61. Epub 2006 Sep 19.

[18] Gibson JR, Beierlein M, Connors BW. Functional properties of electrical synapses between inhibitory interneurons of neocortical layer 4. J Neurophysiol. 2005 Jan;93(1):467-80. Epub 2004 Aug 18.

[19] Golomb D, Hansel D, Shraiman B, Sompolinsky H. Clustering in globally coupled phase oscillators. Phys Rev A. 1992 Mar 15;45(6):3516-3530.

[20] Golomb D, Donner K, Shacham L, Shlosberg D, Amitai Y, Hansel D. Mechanisms of firing patterns in fast-spiking cortical interneurons. PLoS Comput Biol. 2007 Aug;3(8):e156. Epub 2007 Jun 20.

[21] Goldberg JA, Deister CA, Wilson CJ. Response properties and synchronization of rhythmically firing dendritic neurons.J Neurophysiol. 2007 Jan;97(1):208-19. Epub 2006 Sep 6.

[22] Guckenheimer J, Haiduc R (2005), *Canards at folded nodes*, Mosc. Math. J., **5**: 91-103.

[23] Guckenheimer J, Harris-Warrick R, Peck J, Willms A (1997), *Bifurcation, bursting, and spike frequency adaptation*, J. Comp. Neurosci. **4**: 257-277.

[24] Guckenheimer J. (2008), Return maps of folded nodes and folded saddle-nodes, Chaos 18, 015108.

[25] Guckenheimer J (2008), Singular Hopf bifurcation in systems with two slow variables, preprint.

[26] Gurel-Kazanci, F and Ermentrout, GB, Wave Formation Through the Interactions Between Clustered States and Local Coupling in Arrays of Neural Oscillator, (to appear SIADS)

[27] Gutkin BS, Ermentrout GB, Reyes AD. Phase-response curves give the responses of neurons to transient inputs. J Neurophysiol. 2005 Aug;94(2):1623-35. Epub 2005 Apr 13.

[28] Hansel D, Mato G, Meunier C. Clustering and slow switching in globally coupled phase oscillators. Phys Rev E 1993 Nov;48(5):3470-3477.

[29] Hansel D, Mato G, Meunier C. Synchrony in excitatory neural networks. Neural Comput. 1995 Mar;7(2):307-37.

[30] Izhikevich E.M. (2001) Synchronization of Elliptic Bursters. SIAM Review, 43:315-344

[31] Izhikevich E.M. (2007) Dynamical Systems in Neuroscience: The Geometry of Excitability and Bursting. The MIT Press, Cambridge.

[32] Jeong HY, Gutkin B. Synchrony of neuronal oscillations controlled by GABAergic reversal potentials. Neural Comput. 2007 Mar;19(3):706-29.

[33] Kopell N, Ermentrout B. (2004) Chemical and electrical synapses perform complementary roles in the synchronization of interneuronal networks. PNAS 101:15482-7.

[34] Krupa M., Popovic N., Kopell N., Rotstein H. (2008), Mixed-mode oscillations in a three time-scale model for the dopaminergic neuron, Chaos 18, 015106.

[35] Krupa M, Wechselberger M (2008), Local analysis near a folded saddle-node, preprint.
[36] Kuramoto, Y., Chemical Oscillations, Waves, and Turbulence, Springer, Berlin, 1984
[37] Lewis TJ, Rinzel J. Dynamics of spiking neurons connected by both inhibitory and electrical coupling. J Comput Neurosci. 2003 May-Jun;14(3):283-309.
[38] Mancilla JG, Lewis TJ, Pinto DJ, Rinzel J, Connors BW. Synchronization of electrically coupled pairs of inhibitory interneurons in neocortex. J Neurosci. 2007 Feb 21;27(8):2058-73
[39] Milik A, Szmolyan P, Loeffelmann H, Groeller E (1998), *Geometry of mixed-mode oscillations in the 3d autocatalator*, Int. J. Bif. Chaos **8**: 505-519.
[40] Nomura M, Fukai T, Aoyagi T. (2003) Synchrony of fast-spiking interneurons interconnected by GABAergic and electrical synapses, Neural Comp 15:2179-98.
[41] Pfeuty B, Mato G, Golomb D, Hansel D. The combined effects of inhibitory and electrical synapses in synchrony. Neural Comput. 2005 Mar;17(3):633-70.
[42] Rotstein H., Opperman T., White J., Kopell N. (2006) The dynamic structure underlying sub-threshold oscillatory activity and the onset of spikes in a model of medial entorhinal cortex stellate cells, J. Comput. Neurosci. 21, 271-292.
[43] Rotstein H., Wechselberger M., Kopell N., Canard induced mixed-mode oscillations in a medial entorhinal cortex layer II stellate cell model, (2007), submitted.
[44] Rubin J., Wechselberger M., Giant Squid - Hidden Canard: the 3D Geometry of the Hodgkin Huxley Model (2007), Biological Cybernetics, Vol. 97, No. 1, 5-32.
[45] Rubin J., Wechselberger M. (2008), The selection of mixed-mode oscillations in a Hodgkin-Huxley model with multiple timescales, Chaos 18, 015105.
[46] Szmolyan P, Wechselberger M (2001), *Canards in* $\mathbb{R}^3$, J. Diff. Eq. **177**: 419-453.
[47] Van Vreeswijk C, Abbott LF, Ermentrout GB. When inhibition not excitation synchronizes neural firing. J Comput Neurosci. 1994 Dec;1(4):313-21.
[48] Wang XJ, Buzski G. Gamma oscillation by synaptic inhibition in a hippocampal interneuronal network model. J Neurosci. 1996 Oct 15;16(20):6402-13.
[49] Wechselberger M., Existence and Bifurcation of Canards in R^3 in the case of a Folded Node, SIAM J. Appl. Dyn. Syst. (2005), Vol. 4, No. 1, 101-139.
[50] Wechselberger M (2007), Canards, Scholarpedia, 2(4):1356.
[51] White JA, Chow CC, Ritt J, Soto-Trevio C, Kopell N (1998) Synchronization and oscillatory dynamics in heterogeneous, mutally inhibited neurons. J Comput Neurosci 5:5-16.